Contract No.:

This manuscript has been authored by Savannah River Nuclear Solutions (SRNS), LLC under Contract No. DE-AC09-08SR22470 with the U.S. Department of Energy (DOE) Office of Environmental Management (EM).

Graphical Table of Contents

A RIGOROUS PROCESS MODELING METHODOLOGY FOR BIOMASS FAST PYROLYSIS WITH AN ENTRAINED-FLOW REACTOR

Benjamin H. Caudle, Maximilian B. Gorensek*, Chau-Chyun Chen

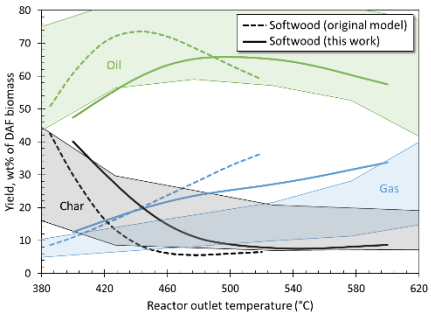

A biomass fast pyrolysis process model, including reactor, separations, and heat recovery, is presented for ready implementation in commercially available process simulation software. The one-dimensional entrained-flow reactor model imposes a rigorous energy balance, providing estimation of temperature profiles, energy utilization, and energy efficiency. Updated reactions and component properties allow for an accurate first principles approach to modeling a wide variety of process conditions and biomass feedstocks.

A RIGOROUS PROCESS MODELING METHODOLOGY FOR BIOMASS FAST PYROLYSIS WITH AN ENTRAINED-FLOW REACTOR

Benjamin H. Caudle[1,2], Maximilian B. Gorensek[3,*], Chau-Chyun Chen[2]

[1]Savannah River Consulting, LLC, 301 Gateway Dr, Aiken, SC 29803

[2]Department of Chemical Engineering, Texas Tech University, PO Box 43121, Lubbock, TX 79409-3121

[3]Renewable and Nuclear Programs, Savannah River National Laboratory, Savannah River Site, 703-41A/225, Aiken, SC 29808

***Corresponding author**

Phone: +1 803 725-1314. E-mail: maximilian.gorensek@srnl.doe.gov.

ORCID

Maximilian B. Gorensek: 0000-0002-4322-9062

Chau-Chyun Chen: 0000-0003-0026-9176

A biomass fast pyrolysis model was developed for implementation in equation-oriented modeling software. Based on a previous framework of coupled 1-dimensional mass, momentum, and heat balance equations, this model includes updated reaction kinetics to provide a more detailed representation of biomass components, intermediates, and products. A recently published derivation of thermodynamic properties for the species in this model has allowed the energy balance around the pyrolysis reactor to be rigorously redefined. With these improvements, the optimum pyrolysis temperature for bio-oil production predicted by the model is increased by up to 50°C, bringing it in line with experimental data and increasing the overall agreement. More importantly, the reactor energy balance is strictly enforced. The resulting model can be used for the design and optimization of biomass fast pyrolysis processes, and comparisons with other options for biomass utilization.

Keywords: Biomass pyrolysis, Reactor model, Entrained-flow, Predictive model, Pyrolysis process flowsheet simulation

Introduction

Fast pyrolysis is a well-developed technique for converting biomass into a useful alternative to fossil fuels. Pyrolysis has long been used to convert biomass into a high-density fuel, utilizing low temperatures (around 400°C) and long residence times to make charcoal.[1] With shorter residence times (1-10 s) and higher temperatures (500-700°C) the product shifts to a liquid bio-oil.[2, 3] This bio-oil has the potential to be refined into a renewable petroleum substitute, but also contains significant amounts of sugars and phenolics that, if separated, can be valuable chemical precursors.[4]

As a distributed feedstock with low mass density, the conversion of biomass to bio-oil is the first step before transportation to a biorefinery. The most common method of conversion today is circulating entrained-flow fast pyrolysis, which is the process modeled here. Due to the complexity of biomass and the pyrolysis reactions, modeling efforts tend to lag process development. The most common models use lumped yields of representative products, with conversion obtained from experimental data.[5] It is also common to use computational fluid dynamics to model the complicated dynamics inside the reactor from first principles.[6] Trendewicz combined aspects of these two approaches into a one-dimensional (1-D) coupled mass, heat, and momentum transfer model[6] that uses the multistep, multicomponent reaction system developed by Ranzi et al.[7] This model avoids the narrow applicability that results from using experimentally-derived conversions while providing a distribution of products sufficient to model downstream processing of the bio-oil. Humbird et al.[8] later integrated the reactor model with commonly used process modeling software.

With the goal of establishing a rigorous process modeling methodology to support heat and mass balance calculations and process design for fast biomass pyrolysis using entrained-flow reactors, this work builds on that of Humbird et al.,[8] incorporating improvements necessary to correct model deficiencies. Specifically, the kinetic scheme is updated with additional components and revised reactions as proposed by Ranzi et al.;[9] the component-based thermophysical properties model reported by Gorensek et al.[10] is incorporated to facilitate heat balance calculations; and the original non-adiabatic heat transfer equations are replaced with rigorous differential enthalpy balance equations. The model includes all unit operations necessary for a biomass to bio-oil processing plant, including reactor, separations, and heat generation by combustion of by-products.

Materials and Methods

Pyrolysis flowsheet model

As with that of Humbird et al.,[8] this model utilizes commercial process modeling software with a custom block for the pyrolysis reactor and standard unit operation blocks for the rest of the plant. While the flowsheet model could be developed with any commercial process simulator, in this case Aspen Plus was used to model the process and Aspen Custom Modeler (ACM) was used to model the entrained-flow reactor.

The process flow diagram of the full plant is shown in Figure 1. Biomass is fed into the pyrolysis reactor, RX-01, along with fluidizing gas at a 1:2 gas-to-biomass mass ratio and sand at a 10.5:1 sand-to-biomass mass ratio. The reactor block has a set mass conversion for each reaction, calculated by the rigorous reactor model in ACM. Pyrolysis products are separated by a 99.9%

efficient cyclone, CY-01, with the solids being sent to the char combustor, RX-02. The vapor products are used to preheat the fluidizing gas in heat exchanger HX-02 and are then further cooled to just above their dew point. They are subsequently partially condensed and separated in a four-stage stripper column, TO-01, operated at 1.72 bar with 90% of the liquid bottoms recycled as the stripping fluid, which enters the column at 16°C. The bio-oil product is taken from the bottoms, leaving the system at 40°C.

It should be noted that the equation-of-state properties model developed by Gorensek et al.[10] predicts two liquid phases in the pyrolysis vapor product condensate, with essentially all of the xylosan and free fatty acid collecting in a separate liquid phase. (If only one liquid phase is allowed, the model keeps xylosan and free fatty acid in the vapor phase, which is unrealistic.) This is not surprising, since a properties model built to characterize gas-solid reactions at pyrolysis conditions cannot be expected to characterize the behavior of complex liquids at near ambient conditions with the same fidelity. Further work is planned to develop a better properties model for bio-oil.

Non-condensable gases are recompressed by CO-02 and split, with the majority used to fluidize the reactor and the balance sent to the char combustor. In the char combustor, solids from the reactor and excess vapor are mixed with air and completely oxidized to water and carbon dioxide. The sand is separated from combustion products with a cyclone and returned to the reactor, passing through a heat exchanger, HX-01, that indirectly controls the temperature of the reactor by controlling the temperature of the sand. Additional heat is recovered by cooling the gaseous combustion products in HX-06.

Each of these blocks is readily available in commercial process modeling software. No customization is required beyond setting the necessary operating parameters mentioned above.

Pyrolysis reactor model

In this model three different phases - biomass, gas, and sand - are tracked separately. The same laboratory-scale reactor is considered as in Humbird et al.:[8] a 4-m long, 8-cm diameter vertically oriented cylinder, with all feeds entering at the bottom. As a 1-D model, properties of the phases are assumed to vary only along the height of the reactor. The particles of both solid phases are modeled with these assumptions: *"(i) particles are identical spheres, (ii) physical properties are isotropic, (iii) particles behave with a lumped heat capacity (uniform temperature), (iv) intraparticle mass transport is not rate limiting, and (v) particle attrition and shrinkage are neglected."*[6] Each phase has its own set of coupled mass, momentum, and energy balance equations, described in detail by Humbird et al.[8]

This model makes use of the updated biomass decomposition kinetics of Ranzi et al.,[9] which incorporate a more detailed evaluation of biomass composition and pyrolysis products. Like the original model,[8] it does not consider secondary gas phase reactions (e.g., Ranzi et al.[11]) which can be important at temperatures as low as 400°C.[12] These could be added for a more complete description in future work. The reactions and their corresponding rate constants (using Humbird et al.'s notation), k_n,

$$k_n = A_n T^{x_n} \exp\left(-\frac{E_n}{RT}\right) \quad (1)$$

are listed in Table 1. As in Humbird et al.'s model,[8] partial trapping of volatile species in a metaplastic phase was disregarded; reactions 21 through 28 in Ranzi et al.[9] were treated as instantaneous and subsumed in reactions 1 through 20 accordingly, with reaction 29 becoming the new reaction 21. The new mechanism of Ranzi et al.[9] changes the description of biomass by splitting hemicellulose into glucomannan (softwood) and xylan (hardwood) and adding the extractives tannin and triglyceride. It also adds the intermediate activated tannin and products acetic acid, acrolein, 3-hydroxypropanal, furfural, anisole, free fatty acid, and high-molecular-weight lignin. In Humbird et al.'s original model,[8] ash is characterized using proximate and ultimate analyses, but here it is treated as a chemical compound (calcium oxide), simplifying the stream structure.

The model also makes use of the thermophysical properties model recently developed by Gorensek et al.,[10] which covers all 49 components appearing in Table 1, of which 20 are not found in commercial simulator databanks. This includes the heat of formation, heat capacity, and solid density of all solid components and the ideal gas enthalpy of formation, critical properties, ideal gas heat capacity, vapor pressure, and acentric factor of all fluid components. The reader is referred to Gorensek et al.[10] for details.

Having a rigorous properties model allows the reactor energy balance to be formulated rigorously. The original heat transfer equations (equations 24-26 in Humbird et al.[8]) are written in terms of the spatial derivatives of the phase temperatures, use fixed values for heat capacities and heats of reaction that differ from the actual temperature-dependent values, do not account for the heat effects of mass transfer between phases, and as a result do not satisfy an energy balance. The new heat transfer equations are formulated in terms of the spatial derivatives of the phase enthalpy fluxes. The three individual phases maintain an enthalpy balance, tracking enthalpy as it passes between the phases due to heat and mass transfer and using the resulting phase enthalpy fluxes to solve for temperature implicitly. Most importantly, the overall reactor energy balance is always satisfied.

The new heat transfer equations are

Biomass phase:

$$\frac{\mathrm{d}Q_\mathrm{b}}{\mathrm{d}z} = h_{\mathrm{b-g}}\left(T_\mathrm{g} - T_\mathrm{b}\right) - \sum_{i}^{\substack{\text{all volatile}\\ \text{products}}} h_i^* \frac{\mathrm{d}}{\mathrm{d}z}\dot{m}_{\mathrm{g},i} \tag{2}$$

Gas phase:

$$\frac{\mathrm{d}Q_\mathrm{g}}{\mathrm{d}z} = h_{\mathrm{s-g}}\left(T_\mathrm{s} - T_\mathrm{g}\right) + h_{\mathrm{b-g}}\left(T_\mathrm{b} - T_\mathrm{g}\right) + \sum_{i}^{\substack{\text{all volatile}\\ \text{products}}} h_i^* \frac{\mathrm{d}}{\mathrm{d}z}\dot{m}_{\mathrm{g},i} \tag{3}$$

Sand phase:

$$\frac{\mathrm{d}Q_\mathrm{s}}{\mathrm{d}z} = h_{\mathrm{s-g}}\left(T_\mathrm{g} - T_\mathrm{s}\right) \tag{4}$$

where Q_p is the enthalpy flux [W/m^2] of phase p (p = b, g, s). It is easy to see that adding all three equations together gives the desired result

$$\frac{dQ_g}{dz} + \frac{dQ_b}{dz} + \frac{dQ_s}{dz} = 0 \tag{5}$$

thereby guaranteeing an energy balance. Enthalpy flux is calculated as

$$Q_p = H_p \phi_p, \tag{6}$$

where H_p is the mass enthalpy [J/kg] and ϕ_p the mass flux [kg/(m^2·s)] of phase p. H_p is a function of local phase temperature, pressure, and composition, which can be calculated from the component-based properties model of Gorensek et al.[10]. The pure component mass enthalpy of volatile species i, h_i^* [J/kg], is also calculated from the properties model, at the temperature of the biomass phase from which it is released. Finally, $\dot{m}_{g,i}$ is the instantaneous mass flow rate [kg/s] of species i in the gas phase, z is the height above the reactor inlet [m], h_{s-g} and h_{b-g} are the heat transfer coefficients per unit height [W/(m^3·K)] for sand-to-gas and biomass-to-gas heat transfer, respectively, and T_a is the temperature [K] of phase a. The correlation for h_{s-g} and h_{b-g} can be found in Humbird et al.,[8] albeit with a missing exponent (d_s should be d_s^2) in the denominator.[6] Equations (2), (3), and (4) replace equations 24-26 in Humbird et al.[8] and require the addition of three instances of equation (6), one for each phase. A complete set of model equations is provided in the Supporting Information.

A few other differences from the original model should be noted. The discretization of the reactor is broken up into five sections of decreasing resolution starting from the inlet: the first is 1 cm high with 1-mm segments, the second 2 cm high with 2-mm segments, the third 7 cm high with 5-mm segments, the fourth 90 cm high with 1-cm segments, and the fifth 3 m high with 10-cm segments. This results in 154 segments, achieving the highest resolution in the first few centimeters where the most significant heat transfer and most of the pyrolysis reactions take place.

With solids present, the built-in capacity to integrate the ACM reactor model with Aspen Plus becomes challenging. Even if integrated successfully, convergence times have been much longer than either model is able to achieve individually. To circumvent these problems, the two models are tied together with an Excel spreadsheet that has dynamic links to both. The spreadsheet acts as an interface for setting process conditions, including reactor temperature, pressure, height and diameter, biomass composition and feed rate, sand/biomass feed ratio, and gas/biomass feed ratio. These inputs are connected to the Aspen Plus model, and simple equations link the necessary inputs of each model with the outputs of the other. By alternately running the two models, a converged solution can be obtained in a matter of minutes.

Results

To assess the effects of the model improvements and new kinetics and thermophysical properties, the model was run at various pyrolysis temperatures under conditions outlined by Humbird et al.[8] A direct comparison with identical feedstock compositions was not possible because the original model does not allow for the presence of extractives while the new one relies on them for complete characterization of biomass. The "base case" in that work assumed a

softwood feedstock for which no extractive content was provided. The Supporting Information for a recent publication by Debiagi et al.[13] tabulates biochemical compositions including extractives for a variety of biomass sources, from which untreated Douglas fir wood was chosen as being closest to the base case feedstock composition. This composition was used in the new model to generate a new base case stream table (Table 2), which can be compared to Humbird et al.'s.[8] A detailed description of the new base case is provided in the Supporting Information.

As in the original, the pyrolysis reactor outlet temperature is 500°C and the three feed streams are the same except for the biomass composition, which includes extractives, and the sand temperature, which is adjusted to achieve a 500°C reactor outlet temperature. More bio-oil (55.8 instead of 51.2 kg/h) and less gas product (20.7 instead of 26.6 kg/h) is produced than in the original. This kind of difference is not unexpected since a different kinetic model is being used - Humbird et al.[8] utilized a modified, older version of Ranzi et al.'s kinetic model[14] - and the original model did not maintain an energy balance.

Figure 2 demonstrates the ability of the reactor model to provide profiles for internal variables. As seen in previous work (Humbird et al.[8]) the majority of the heat transfer and biomass reaction occur in the first meter of the reactor. This validates the choice of segment spacing used in the numerical differentiation. An additional feature included in the revised model is a set of equations, included in the Supporting Information, that calculate the individual residence time of each of the three phases. As expected, the fluidizing gas has the shortest residence time, 1.05 seconds, while the biomass has a residence time of 2.63 s and the sand a residence time of 3.88 s. These values are consistent with those calculated by Trendewicz[6] and with typical values for fast pyrolysis from the literature.[3, 15] The ability to quantify the biomass residence time allows for further fine-tuning of reactor operation.

A biochemical composition including extractives could also be found in the Supporting Information for Debiagi et al.[13] for switchgrass, but a similarly analogous species could not be found for corn stover. Consequently, comparisons with Humbird et al.'s other results[8] could only be drawn for softwood and switchgrass. As shown in Figure 3, the dry, ash-free (DAF) basis bio-oil yield curves of the new model when plotted against pyrolysis temperature are shifted to the right of those in the original, which is in agreement with the generally accepted optimum temperature for bio-oil production of around 500° C.[16]

Additional results are shown in Figure 4, which plots the DAF biomass-basis yields of bio-oil and non-condensable gas from the quench loop and char from the cyclone for softwood feedstock as functions of pyrolysis temperature. Figure 4(a) further breaks down the bio-oil yield, attributing bio-oil components to their carbohydrate, lignin, or extractive origin (the balance is water), while Figure 4(b) compares the yields to bands of typical experimental results taken from Calonaci et al.[16] The results are consistent with the base case observation that bio-oil production is higher and gas production lower at 500°C with the new model compared to the original. In general, the new model fits the experimental bands better than the original. The oil yield predicted by the new model falls within the experimental band over nearly the entire 400 to 600°C temperature range, while that from the original model appears to fall below the lower bound at temperatures above 530°C. Both models overestimate the amount of noncondensing gas collected from the reactor in comparison to the experimental band, although the new model tracks it more closely. As for char formation, the new model overlaps a wider region of the experimental band than the original. Thus, it is clear that the new model has a better fit to Calonaci et al.'s data[16] than the original.

Because the process outside of the pyrolysis reactor is fully modeled, it is possible to carry out a parametric study encompassing the reactor and auxiliary operations. The results of a simple study illustrating the effects of reactor temperature, reactor pressure, biomass feed rate, sand/biomass ratio, gas/biomass ratio, and reactor diameter are included here. Using the base-case shown in Table 2 as a starting point, those variables were individually varied by approximately ±20% and ±40%. The reactor temperature was not able to go far below 340° C without making significant alterations to the absorber portion of the model, and so that was the minimum temperature used in this study.

Table 3 includes raw results for all trials. The effects of sand/biomass ratio and gas/biomass ratio were insignificant compared to those of the other four variables, and so were excluded from the figures that follow.

The effect on product distribution is illustrated by Figure 5. Reactor temperature, pressure, diameter, and feed rate all have a significant effect on the proportion of bio-oil, gas, and char produced. Temperature behaves as seen in previous diagrams. Holding all other variables constant, reactor diameter is proportional to the residence time of biomass within the reactor. This explains why a narrower reactor favors solids in the form of unreacted biomass and intermediates, while a wider reactor produces more noncondensing gas. The feed rate is inversely proportional to residence time, and so shows the same trends in reverse. Since feed rate is directly proportional to residence time while reactor diameter is quadratically proportional, the effects of equal perturbation are less severe. The effect of pressure is more complicated, as the pressure within the reactor limits the pressure of the absorber column. It also indirectly affects the residence time of the reactor due to its inverse relationship to the volumetric density of the vapor phase. It seems that the latter effect predominates, as the trends for pressure follow those of reactor diameter.

Because the power draw of the air compressor CO-01 is an order of magnitude larger than that of the vapor product compressor CO-02, many process changes have little effect on the total compressor power draw per unit mass of bio-oil. The exceptions are system pressure, which requires a large change in the supply of power to CO-01, and feed rate, which has a positive effect on the per-unit-mass-bio-oil efficiency of the process. The amount of high-pressure steam generated is directly correlated with the bio-oil production rate. With all unwanted products sent to the combustor and that energy recovered as steam, a decrease in bio-oil production increases the amount of steam produced per unit mass of bio-oil. The use of cooling and chilled water tracks with the production of gas, reflecting the increased load on the absorber column.

Discussion

The leftward shift of the original model prediction of the pyrolysis temperature at which bio-oil production is maximized was attributed by its authors to inclusion in the total bio-oil production of partially reacted carbohydrates and lignins, which predominate at lower temperatures and which would be expected to form tars or remain with the char rather than exit the process as bio-oil.[8] However, exclusion of these species does not fully make up the difference and the lack of an energy balance may provide another explanation. When the original model base case was run, the outlet temperature calculated from the original heat transfer equations was 499.3°C, whereas the temperature calculated from an energy balance around the reactor was found to be 556.9°C. Repeating the simulation using Gorensek et al.'s property parameters and updated

enthalpies of reaction,[10] the heat transfer equations predicted a reactor outlet temperature of only 474.9°C, while the energy balance result was 509.9°C. The nearly 25°C difference in outlet temperatures calculated from the heat transfer equations for the two cases (499.3°C versus 474.9°C) is to be expected as the corrected enthalpies of reaction are more endothermic than those used by Humbird et al.[8] More importantly, not imposing an energy balance on the pyrolysis reactor leads to a large departure of the reactor outlet temperature predicted by the heat transfer equations from that which satisfies the energy balance. Furthermore, while the flowsheet model treats the pyrolysis reactor as adiabatic, with all of the necessary heat provided by the hot sand, the original reactor model is not adiabatic, leaving an implied heat flow unaccounted for. Thus, the temperatures used in Humbird et al.'s[8] analyses are not reliable, and are expected to significantly underestimate the outlet temperature of the reactor for a given set of inlet conditions.

Both the original and the new model predict a higher ratio of gas-to-liquid products compared to Calonaci et al.'s ranges of experimental results,[16] although the new model follows the trends in the experimental data more closely, especially at higher temperatures. The high gas-to-liquid ratios may be due to secondary gas phase reactions that occur prior to quenching, creating additional condensable species which neither model considers.

The prediction of two immiscible liquid phases occurring in the bio-oil is an unintended consequence of using a cubic equation of state to characterize compounds that are solids in their pure form at bio-oil temperatures (e.g., xylosan, which is a solid at 298.15K that is soluble in water). The properties model developed by Gorensek et al.[10] is suited for pyrolysis conditions, where most of the pyrolysis products are in the vapor phase. While it can be used at lower temperatures as it is here, the results for the low-temperature flowsheet operations need to be viewed *cum grano salis.* This is a problem that will be addressed in future work.

Conclusions

Built on the work of Humbird et al.,[8] this model presents the recommended modeling methodology for biomass pyrolysis process modeling activities. Updated properties that cover every species in the model allow for a rigorous enthalpy balance that satisfies the energy balance. The resulting performance curves agree with experimental observation and closely align with the product distribution regions compiled by Calonaci et al.[16] The model is robust enough to carry out sensitivity studies on a number of process variables, including temperature, pressure, feed rates, recycle rates, and reactor dimensions. Such studies can support development, analysis, and optimization of biomass pyrolysis processes that include entrained-flow reactors. The model should set the foundation for rigorous process modeling of fast biomass pyrolysis using fluidized bed reactors.

Acknowledgments

Funding support was provided by the US Department of Energy under grant DE-EE0007888-02-7. C.-C.C. gratefully acknowledges the financial support of the Jack Maddox Distinguished Engineering Chair Professorship in Sustainable Energy, sponsored by the J.F Maddox Foundation. SRNL is operated for the DOE's Office of Environmental Management (DOE-EM) by Savannah River Nuclear Solutions, LLC, under Contract DE-A C09-08SR22470.

Disclaimer

This report was prepared as an account of work sponsored by an agency of the United States Government. Neither the United States Government nor any agency thereof, nor any of their employees, makes any warranty, express or implied, or assumes any legal liability or responsibility for the accuracy, completeness, or usefulness of any information, apparatus, product, or process disclosed, or represents that its use would not infringe privately owned rights. Reference herein to any specific commercial product, process, or service by trade name, trademark, manufacturer, or otherwise does not necessarily constitute or imply its endorsement, recommendation, or favoring by the United States Government or any agency thereof. The views and opinions of authors expressed herein do not necessarily state or reflect those of the United States Government or any agency thereof.

Conflict of Interest

The authors declare no competing financial interest.

Author Contributions

The manuscript was written through contributions of all authors. All authors have given approval to the final version of the manuscript. All authors contributed equally.

Literature Cited

1. Bridgwater, A. V. Biomass Pyrolysis. http://www.ieabioenergy.com/wp-content/uploads/2013/10/Task-34-Booklet.pdf (April 12, 2019),
2. Bridgwater, A. V., Review of fast pyrolysis of biomass and product upgrading. *Biomass and Bioenergy* **2012,** 38, 68-94.
3. Mohan, D.; Pittman, C. U.; Steele, P. H., Pyrolysis of Wood/Biomass for Bio-oil: A Critical Review. *Energy & Fuels* **2006,** 20, (3), 848-889.
4. Venderbosch, R.; Prins, W., Fast pyrolysis technology development. *Biofuels, Bioproducts and Biorefining* **2010,** 4, (2), 178-208.
5. Miller, R. S.; Bellan, J., A Generalized Biomass Pyrolysis Model Based on Superimposed Cellulose, Hemicellulose and Lignin Kinetics. *Combustion Science and Technology* **1997,** 126, (1-6), 97-137.
6. Trendewicz, A. A. Development of a circulating fluidized bed reactor model for the fast pyrolysis of biomass for process simulation. Colorado School of Mines, Golden, CO, 2015.
7. Ranzi, E.; Cuoci, A.; Faravelli, T.; Frassoldati, A.; Migliavacca, G.; Pierucci, S.; Sommariva, S., Chemical Kinetics of Biomass Pyrolysis. *Energy & Fuels* **2008,** 22, (6), 4292-4300.
8. Humbird, D.; Trendewicz, A.; Braun, R.; Dutta, A., One-Dimensional Biomass Fast Pyrolysis Model with Reaction Kinetics Integrated in an Aspen Plus Biorefinery Process Model. *ACS Sustainable Chemistry & Engineering* **2017,** 5, (3), 2463-2470.

9. Ranzi, E.; Debiagi, P. E. A.; Frassoldati, A., Mathematical Modeling of Fast Biomass Pyrolysis and Bio-Oil Formation. Note I: Kinetic Mechanism of Biomass Pyrolysis. *ACS Sustainable Chemistry & Engineering* **2017,** 5, (4), 2867-2881.
10. Gorensek, M. B.; Shukre, R.; Chen, C.-C., Development of a thermophysical properties model for flowsheet simulation of biomass pyrolysis processes. *ACS Sustainable Chemistry & Engineering* **2019,** 7, (9), 9017-27.
11. Ranzi, E.; Debiagi, P. E. A.; Frassoldati, A., Mathematical Modeling of Fast Biomass Pyrolysis and Bio-Oil Formation. Note II: Secondary Gas-Phase Reactions and Bio-Oil Formation. *ACS Sustainable Chemistry & Engineering* **2017,** 5, (4), 2882-2896.
12. Hoekstra, E.; Westerhof, R. J. M.; Brilman, W.; Van Swaaij, W. P. M.; Kersten, S. R. A.; Hogendoorn, K. J. A.; Windt, M., Heterogeneous and homogeneous reactions of pyrolysis vapors from pine wood. *AIChE Journal* **2012,** 58, (9), 2830-2842.
13. Debiagi, P. E. A.; Pecchi, C.; Gentile, G.; Frassoldati, A.; Cuoci, A.; Faravelli, T.; Ranzi, E., Extractives Extend the Applicability of Multistep Kinetic Scheme of Biomass Pyrolysis. *Energy & Fuels* **2015,** 29, (10), 6544-6555.
14. Ranzi, E.; Corbetta, M.; Manenti, F.; Pierucci, S., Kinetic modeling of the thermal degradation and combustion of biomass. *Chemical Engineering Science* **2014,** 110, 2-12.
15. Ringer, M.; Putsche, V.; Scahill, J. *Large-Scale Pyrolysis Oil Production: A Technology Assessment and Economic Analysis NREL/TP-510-37779*; National Renewable Energy Laboratory: Golden, CO, November 2006.
16. Calonaci, M.; Grana, R.; Barker Hemings, E.; Bozzano, G.; Dente, M.; Ranzi, E., Comprehensive Kinetic Modeling Study of Bio-oil Formation from Fast Pyrolysis of Biomass. *Energy & Fuels* **2010,** 24, (10), 5727-5734.

Table 1 Biomass pyrolysis reaction mechanism adapted from Ranzi et al.[9] (compound names defined by Gorensek et al.[10])

Reaction No., *n*	**Reaction**	A_n [$K^{-x_n} \cdot s^{-1}$]	x_n	E_n [kcal/kmol]
1	CELL → CELLA	1.5×10^{14}	0	47000
2	CELLA → 0.4 HAA + 0.05 GLYOX + 0.15 CH3CHO + 0.25 HMFU + 0.35 ALD3 + 0.15 CH3OH + 0.3 CH2O + 0.61 CO + 0.36 CO2 + 0.25 H2 + 0.93 H2O + 0.02 HCOOH + 0.05 C3H6O2 + 0.05 CH4 + 0.61 CHAR	2.5×10^{6}	0	19100
3	CELLA → LVG	3.3	1	10000
4	CELL → 5 H2O + 6 CHAR	6×10^{7}	0	31000
5	GMSW → 0.7 HCE1 + 0.3 HCE2	1×10^{10}	0	31000
6	XYHW → 0.35 HCE1 + 0.65 HCE2	1×10^{10}	0	28500
7	HCE1 → 0.6 XYLAN + 0.2 C3H6O2 + 0.12 GLYOX + 0.2 FURF + 0.4 H2O + 0.08 H2 + 0.16 CO	3	1	11000
8	HCE1 → 0.4 H2O + 0.8 CO2 + 0.05 HCOOH + 1.6 CO + 1.25 H2 + 0.3 CH2O + 0.625 CH4 + 0.375 C2H4 + 0.875 CHAR	1.8×10^{-3}	1	3000
9	HCE2 → 0.2 H2O + CO + 0.575 CO2 + 0.4 CH2O + 0.1 C2H5OH + 0.05 HAA + 0.35 ACAC + 0.025 HCOOH + 0.25 CH4 + 0.3 CH3OH + 0.225 C2H4 + 0.725 H2 + CHAR	5×10^{9}	0	31500
10	LIGC → 0.35 LIGCC + 0.1 COUMARYL + 0.08 PHENOL + 0.41 C2H4 + H2O + 1.02 CO + 0.7 H2 + 0.3 CH2O + 0.495 CH4 + 5.735 CHAR	1×10^{11}	0	37200
11	LIGH → LIGOH + 0.5 ALD3 + 0.5 C2H4 + 0.2 HAA + 0.1 CO + 0.1 H2	6.7×10^{12}	0	37500
12	LIGO → LIGOH + CO2	3.3×10^{8}	0	25500
13	LIGCC → 0.3 COUMARYL + 0.2 PHENOL + 0.35 HAA + 0.7 H2O + 0.65 CH4 + 0.6 C2H4 + H2 + 1.8 CO + 6.75 CHAR	1×10^{4}	0	24800
14	LIGOH → 0.9 LIG + H2O + 0.45 CH4 + 0.9 CH3OH + 0.9 H2 + 0.05 CO2 + 2.1 CO + 0.05 HCOOH + 0.2 C2H4 + 0.025 HMWL + 0.1 ACROL + 4.25 CHAR	1×10^{8}	0	30000
15	LIG → 0.7 FE2MACR + 0.3 ANISOLE + 0.6 CO + 0.3 CH3CHO	4	1	12000
16	LIG → 0.6 H2O + 2.6 CO + 0.6 CH4 + 0.4 CH2O + 0.5 C2H4 + 0.4 CH3OH + 2 H2 + 6 CHAR	8.3×10^{-2}	1	8000
17	LIG → 0.6 H2O + 2.6 CO + 1.1 CH4 + 0.4 CH2O + C2H4 + 0.4 CH3OH + 4.5 CHAR	1×10^{7}	0	24300
18	TGL → ACROL + 3 FFA	7×10^{12}	0	45700
19	TANN → PHENOL + CO + H2O + ITANN	20	0	10000
20	ITANN → 5 CHAR + 3 CO + H2O + H2	1×10^{3}	0	25000
21	H2O → H2OL	1	1	8000

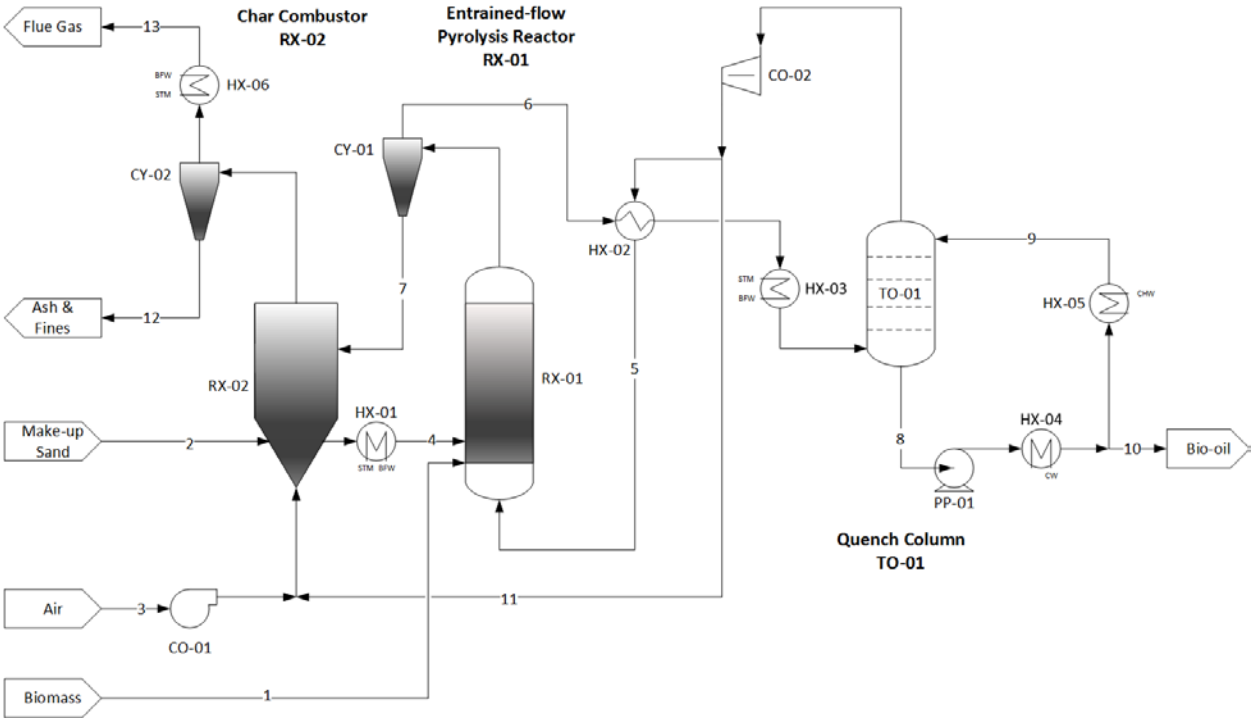

Figure 1 Process flow diagram for the fast pyrolysis flowsheet

Table 2 Stream table for base case

Stream			**01**		**02**		**03**		**04**		**05**		**06**		**07**		**08**		**09**		**10**		**11**		**12**		**13**	
Description			Biomass Feed		Sand Make-up		Combustor Air		Sand Feed		Fluidizing Gas		Pyrolysis Vapor		Pyrolysis Solids		Absorber Bottoms		Quench Oil		Bio Oil Product		Gas Product		Ash + Fines		Flue Gas	
Temperature (°C)			100		25		25		624		397		500.3		500.3		83.2		16.0		40.0		69.5		777.2		98.0	
Pressure (bar)			2.30		2.30		1.01		2.30		2.30		2.28		2.28		1.81		1.72		1.77		2.55		2.30		1.01	
Total Flow (kg/h)			83.3		1.7		325.0		855.7		41.6		118.2		862.4		558.5		502.6		55.8		20.7		1.2		352.9	
ID	**Component Name**	**Formula**	kg/h	wt%	kg/h	wt%	kg/h	wt%	kg/h	wt%	kg/h	wt%	kg/h	wt%	kg/h	wt%	kg/h	wt%	kg/h	wt%	kg/h	wt%	kg/h	wt%	kg/h	wt%	kg/h	wt%
LIG	Secondary Lignin Intermediate	$[C_{11}H_{12}O_4]_n$	–	–	–	–	–	–	–	–	–	–	0.6	0.5	0.0	0.0	5.9	1.1	5.3	1.1	0.6	1.1	–	–	–	–	–	–
TANN	Tannin	$[C_{15}H_{12}O_7]_n$	1.0	1.2	–	–	–	–	–	–	–	–	0.0	0.0	1.0	0.1	0.0	0.0	0.0	0.0	0.0	0.0	–	–	–	–	–	–
LIGC	C-rich Lignin	$[C_{15}H_{14}O_4]_n$	3.8	4.6	–	–	–	–	–	–	–	–	0.0	0.0	0.2	0.0	0.0	0.0	0.0	0.0	0.0	0.0	–	–	–	–	–	–
LIGCC	C-rich Lignin Intermediate	$[C_{15}H_{14}O_4]_n$	–	–	–	–	–	–	–	–	–	–	1.3	1.1	0.0	0.0	12.7	2.3	11.5	2.3	1.3	2.3	–	–	–	–	–	–
LIGOH	H/O-rich Lignin Intermediate	$[C_{19}H_{22}O_8]_n$	–	–	–	–	–	–	–	–	–	–	11.3	9.6	0.0	0.0	113.3	20.3	102.0	20.3	11.3	20.3	–	–	–	–	–	–
LIGO	O-rich Lignin	$[C_{20}H_{22}O_{10}]_n$	8.9	10.6	–	–	–	–	–	–	–	–	0.0	0.0	0.0	0.0	0.0	0.0	0.0	0.0	0.0	0.0	–	–	–	–	–	–
LIGH	H-rich Lignin	$[C_{22}H_{28}O_9]_n$	9.8	11.8	–	–	–	–	–	–	–	–	0.0	0.0	0.0	0.0	0.0	0.0	0.0	0.0	0.0	0.0	–	–	–	–	–	–
GMSW	Glucomannan Hemicellulose	$[C_5H_8O_4]_n$	17.9	21.5	–	–	–	–	–	–	–	–	0.0	0.0	0.0	0.0	0.0	0.0	0.0	0.0	0.0	0.0	–	–	–	–	–	–
XYHW	Xylan Hemicellulose	$[C_5H_8O_4]_n$	–	–	–	–	–	–	–	–	–	–	–	–	–	–	–	–	–	–	–	–	–	–	–	–	–	–
HCE1	Activated Hemicellulose 1	$[C_5H_8O_4]_n$	–	–	–	–	–	–	–	–	–	–	0.6	0.5	0.0	0.0	6.2	1.1	5.6	1.1	0.6	1.1	–	–	–	–	–	–
HCE2	Activated Hemicellulose 2	$[C_5H_8O_4]_n$	–	–	–	–	–	–	–	–	–	–	0.0	0.0	0.0	0.0	0.1	0.0	0.1	0.0	0.0	0.0	–	–	–	–	–	–
CELL	Cellulose	$[C_6H_{10}O_5]_n$	35.8	43.0	–	–	–	–	–	–	–	–	0.0	0.0	0.1	0.0	0.0	0.0	0.0	0.0	0.0	0.0	–	–	–	–	–	–
CELLA	Activated Cellulose	$[C_6H_{10}O_5]_n$	–	–	–	–	–	–	–	–	–	–	0.1	0.1	0.0	0.0	0.7	0.1	0.6	0.1	0.1	0.1	–	–	–	–	–	–
AR	Argon	Ar	–	–	–	–	4.2	1.3	–	–	–	–	–	–	–	–	–	–	–	–	–	–	–	–	–	–	4.2	1.2
CHAR	Char (Carbon)	C	–	–	–	–	–	–	–	–	–	–	0.0	0.0	4.0	0.5	0.0	0.0	0.0	0.0	0.0	0.0	–	–	–	–	–	–
FE2MACR	Sinapyl Aldehyde	$C_{11}H_{12}O_4$	–	–	–	–	–	–	–	–	0.0	0.0	0.6	0.5	–	–	6.1	1.1	5.5	1.1	0.6	1.1	0.0	0.0	–	–	–	–
FFA	Free Fatty (Linoleic) Acid	$C_{18}H_{32}O_2$	–	–	–	–	–	–	–	–	0.0	0.0	2.0	1.7	–	–	19.4	3.5	17.5	3.5	1.9	3.5	0.0	0.0	–	–	–	–
HMWL	High Mol. Wt. Lignin	$C_{24}H_{28}O_4$	–	–	–	–	–	–	–	–	–	–	0.1	0.1	0.0	0.0	1.3	0.2	1.1	0.2	0.1	0.2	–	–	–	–	–	–
GLYOX	Glyoxal	$C_2H_2O_2$	–	–	–	–	–	–	–	–	1.3	3.0	2.2	1.9	–	–	3.5	0.6	3.1	0.6	0.3	0.6	0.6	3.0	–	–	–	–
C2H4	Ethylene	C_2H_4	–	–	–	–	–	–	–	–	2.1	5.0	3.1	2.7	–	–	0.0	0.0	0.0	0.0	0.0	0.0	1.0	5.0	–	–	–	–
CH3CHO	Acetaldehyde	C_2H_4O	–	–	–	–	–	–	–	–	1.9	4.7	3.0	2.5	–	–	0.5	0.1	0.4	0.1	0.0	0.1	1.0	4.7	–	–	–	–
ACAC	Acetic Acid	$C_2H_4O_2$	–	–	–	–	–	–	–	–	0.1	0.2	0.9	0.8	–	–	8.2	1.5	7.4	1.5	0.8	1.5	0.0	0.2	–	–	–	–
HAA	Glycol Aldehyde	$C_2H_4O_2$	–	–	–	–	–	–	–	–	0.0	0.0	3.9	3.3	–	–	38.7	6.9	34.8	6.9	3.9	6.9	0.0	0.0	–	–	–	–
C2H5OH	Ethanol	C_2H_6O	–	–	–	–	–	–	–	–	0.1	0.2	0.3	0.2	–	–	1.5	0.3	1.4	0.3	0.2	0.3	0.0	0.2	–	–	–	–
ACROL	Acrolein	C_3H_4O	–	–	–	–	–	–	–	–	0.4	0.9	0.6	0.5	–	–	0.3	0.0	0.2	0.0	0.0	0.0	0.2	0.9	–	–	–	–
ALD3	*n*-Propionaldehyde	C_3H_6O	–	–	–	–	–	–	–	–	6.5	15.7	10.1	8.6	–	–	3.6	0.6	3.2	0.6	0.4	0.6	3.2	15.7	–	–	–	–

Stream			01		02		03		04		05		06		07		08		09		10		11		12		13	
Description			Biomass Feed		Sand Make-up		Combustor Air		Sand Feed		Fluidizing Gas		Pyrolysis Vapor		Pyrolysis Solids		Absorber Bottoms		Quench Oil		Bio Oil Product		Gas Product		Ash + Fines		Flue Gas	
Temperature (°C)			100		25		25		624		397		500.3		500.3		83.2		16.0		40.0		69.5		777.2		98.0	
Pressure (bar)			2.30		2.30		1.01		2.30		2.30		2.28		2.28		1.81		1.72		1.77		2.55		2.30		1.01	
Total Flow (kg/h)			83.3		1.7		325.0		855.7		41.6		118.2		862.4		558.5		502.6		55.8		20.7		1.2		352.9	
ID	**Component Name**	**Formula**	kg/h	wt%	kg/h	wt%	kg/h	wt%	kg/h	wt%	kg/h	wt%	kg/h	wt%	kg/h	wt%	kg/h	wt%	kg/h	wt%	kg/h	wt%	kg/h	wt%	kg/h	wt%	kg/h	wt%
C3H6O2	3-Hydroxypropanal	$C_3H_6O_2$	–	–	–	–	–	–	–	–	0.0	0.0	1.7	1.4	–	–	17.1	3.1	15.4	3.1	1.7	3.1	0.0	0.0	–	–	–	–
TGL	Triglyceride	$C_{57}H_{100}O_7$	4.1	4.9	–	–	–	–	–	–	0.0	0.0	0.0	0.0	2.0	0.2	0.0	0.0	0.0	0.0	0.0	0.0	0.0	0.0	–	–	–	–
FURF	Furfural	$C_5H_4O_2$	–	–	–	–	–	–	–	–	0.0	0.1	1.5	1.3	–	–	15.1	2.7	13.6	2.7	1.5	2.7	0.0	0.1	–	–	–	–
XYLAN	Xylosan	$C_5H_8O_4$	–	–	–	–	–	–	–	–	0.0	0.0	6.3	5.3	–	–	62.6	11.2	56.4	11.2	6.3	11.2	0.0	0.0	–	–	–	–
LVG	Levoglucosan	$C_6H_{10}O_5$	–	–	–	–	–	–	–	–	0.0	0.0	11.3	9.6	–	–	113.0	20.2	101.7	20.2	11.3	20.2	0.0	0.0	–	–	–	–
PHENOL	Phenol	C_6H_6O	–	–	–	–	–	–	–	–	0.0	0.0	0.1	0.1	–	–	1.2	0.2	1.1	0.2	0.1	0.2	0.0	0.0	–	–	–	–
HMFU	5-Hydroxymethyl Furfural	$C_6H_6O_3$	–	–	–	–	–	–	–	–	0.0	0.0	4.6	3.9	–	–	45.8	8.2	41.2	8.2	4.6	8.2	0.0	0.0	–	–	–	–
ANISOLE	Anisole	C_7H_8O	–	–	–	–	–	–	–	–	0.0	0.0	0.2	0.1	–	–	1.3	0.2	1.1	0.2	0.1	0.2	0.0	0.0	–	–	–	–
ITANN	Tannin Intermediate	$C_8H_4O_4$	–	–	–	–	–	–	–	–	–	–	0.0	0.0	0.0	0.0	0.3	0.1	0.3	0.1	0.0	0.1	–	–	–	–	–	–
COUMARYL	*p*-Coumaryl Alcohol	$C_9H_{10}O_2$	–	–	–	–	–	–	–	–	0.0	0.0	0.2	0.2	–	–	2.1	0.4	1.9	0.4	0.2	0.4	0.0	0.0	–	–	–	–
CH2O	Formaldehyde	CH_2O	–	–	–	–	–	–	–	–	4.1	9.8	6.2	5.2	–	–	0.5	0.1	0.4	0.1	0.0	0.1	2.0	9.8	–	–	–	–
HCOOH	Formic Acid	CH_2O_2	–	–	–	–	–	–	–	–	0.1	0.1	0.3	0.3	–	–	2.1	0.4	1.9	0.4	0.2	0.4	0.0	0.1	–	–	–	–
CH4	Methane	CH_4	–	–	–	–	–	–	–	–	1.4	3.3	2.0	1.7	–	–	0.0	0.0	0.0	0.0	0.0	0.0	0.7	3.3	–	–	–	–
CH3OH	Methanol	CH_4O	–	–	–	–	–	–	–	–	0.4	1.0	2.0	1.7	–	–	13.3	2.4	11.9	2.4	1.3	2.4	0.2	1.0	–	–	–	–
CO	Carbon Monoxide	CO	–	–	–	–	–	–	–	–	12.4	29.7	18.5	15.7	–	–	0.1	0.0	0.1	0.0	0.0	0.0	6.2	29.7	–	–	–	–
CO2	Carbon Dioxide	CO_2	–	–	–	–	0.2	0.1	–	–	9.3	22.4	14.0	11.8	–	–	0.2	0.0	0.2	0.0	0.0	0.0	4.6	22.4	–	–	56.7	16.1
ASH	Ash (Calcium Oxide)	CaO	0.4	0.5	–	–	–	–	–	–	–	–	–	–	0.4	0.0	0.0	0.0	0.0	0.0	0.0	0.0	–	–	0.4	30.5	0.0	0.0
H2	Hydrogen	H_2	–	–	–	–	–	–	–	–	0.5	1.1	0.7	0.6	–	–	0.0	0.0	0.0	0.0	0.0	0.0	0.2	1.1	–	–	–	–
H2O	Water	H_2O	–	–	–	–	–	–	–	–	1.2	2.8	7.1	6.0	–	–	53.2	9.5	47.9	9.5	5.3	9.5	0.6	2.8	–	–	13.6	3.9
H2OL	Moisture	H_2O	1.7	2.0	–	–	–	–	–	–	0.0	0.0	0.0	0.0	0.0	0.0	0.0	0.0	0.0	0.0	0.0	0.0	0.0	0.0	–	–	–	–
N2	Nitrogen	N_2	–	–	–	–	245.4	75.5	–	–	–	–	–	–	–	–	–	–	–	–	–	–	–	–	–	–	245.4	69.5
O2	Oxygen	O_2	–	–	–	–	75.2	23.1	–	–	–	–	–	–	–	–	–	–	–	–	–	–	–	–	–	–	33.0	9.3
SAND	Sand (Silica)	SiO_2	–	–	1.7	100.0	–	–	855.7	100.0	–	–	0.9	0.7	854.8	99.1	8.6	1.5	7.7	1.5	0.9	1.5	–	–	0.9	69.5	–	–

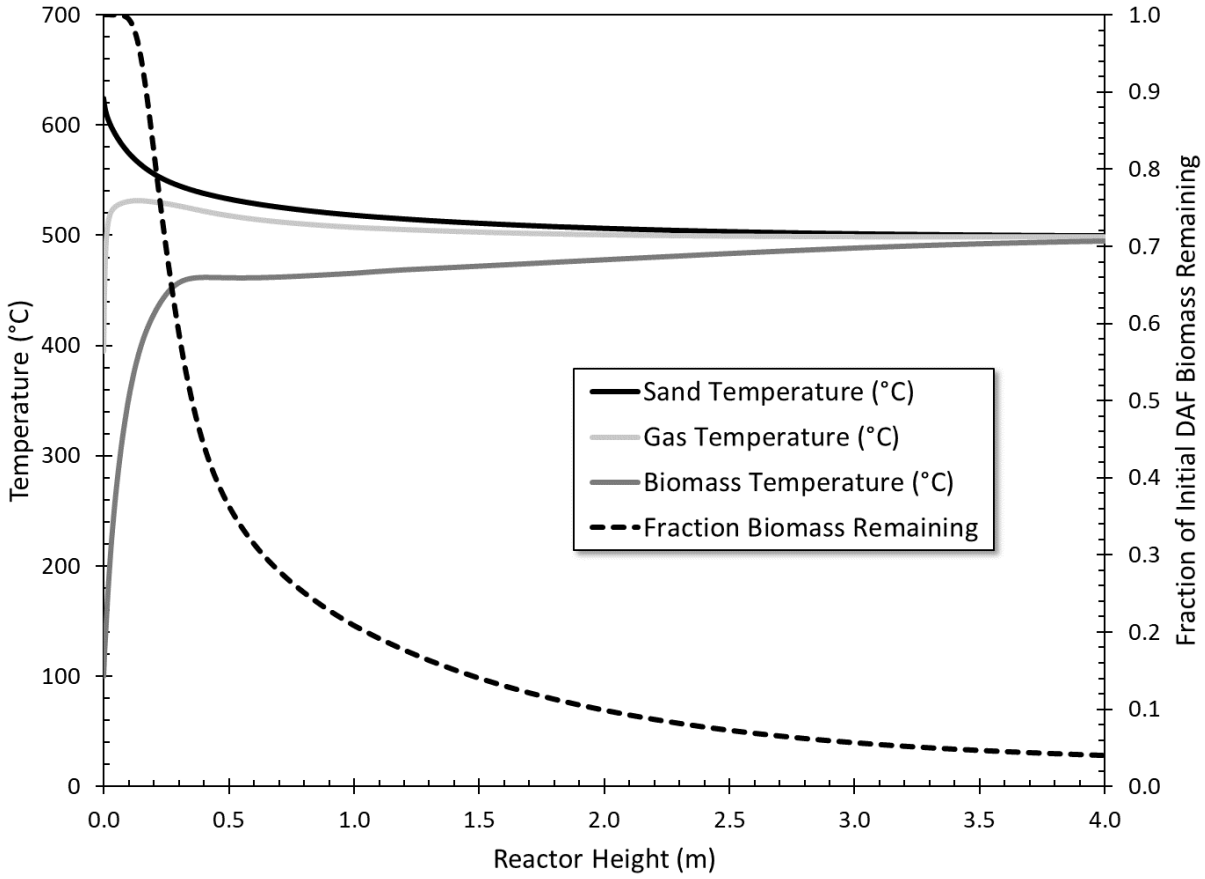

Figure 2 Reactor temperature and biomass conversion profiles for the base case.

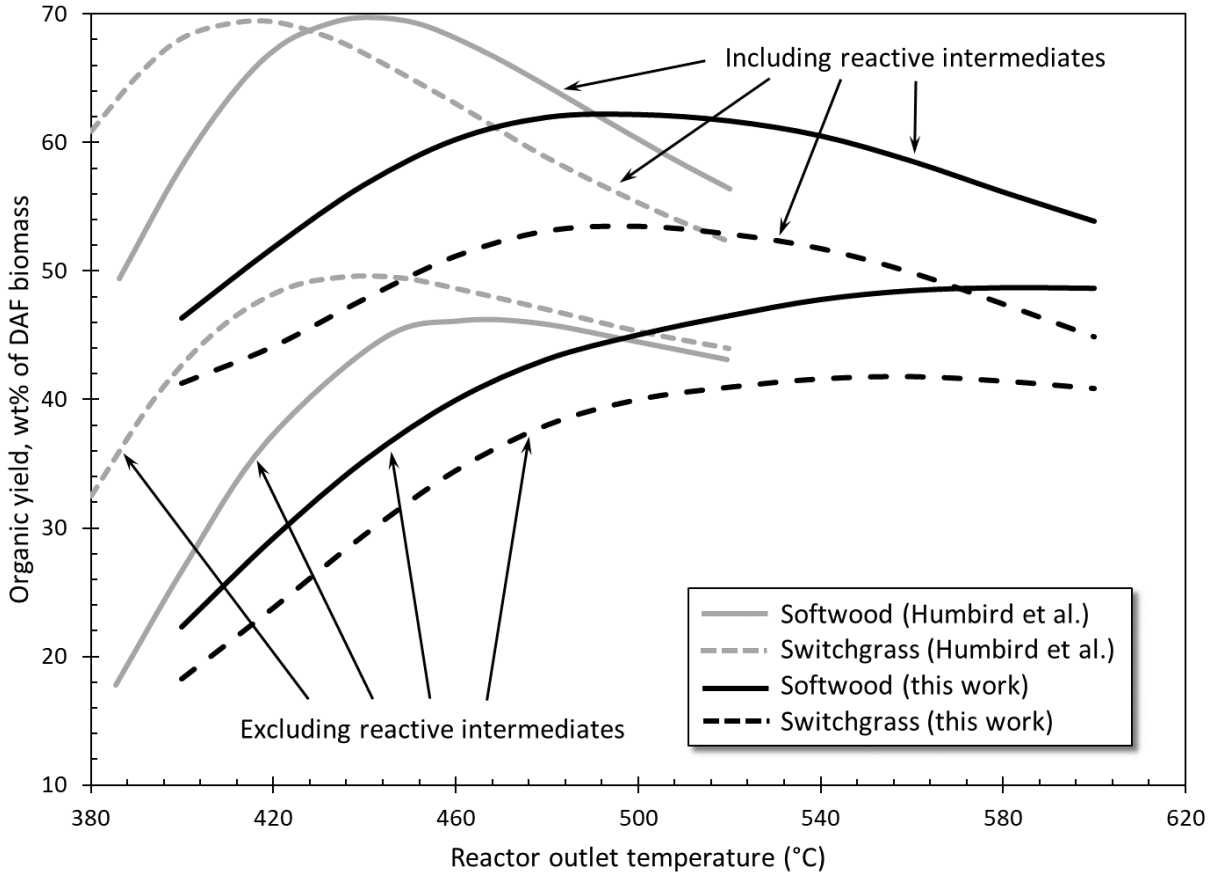

Figure 3 Comparison between organic bio-oil yields for two different feedstocks predicted by the Humbird et al. model[8] and the new model. Upper curves consider all recovered organic material, while lower curves exclude reactive intermediates that likely form tar instead.

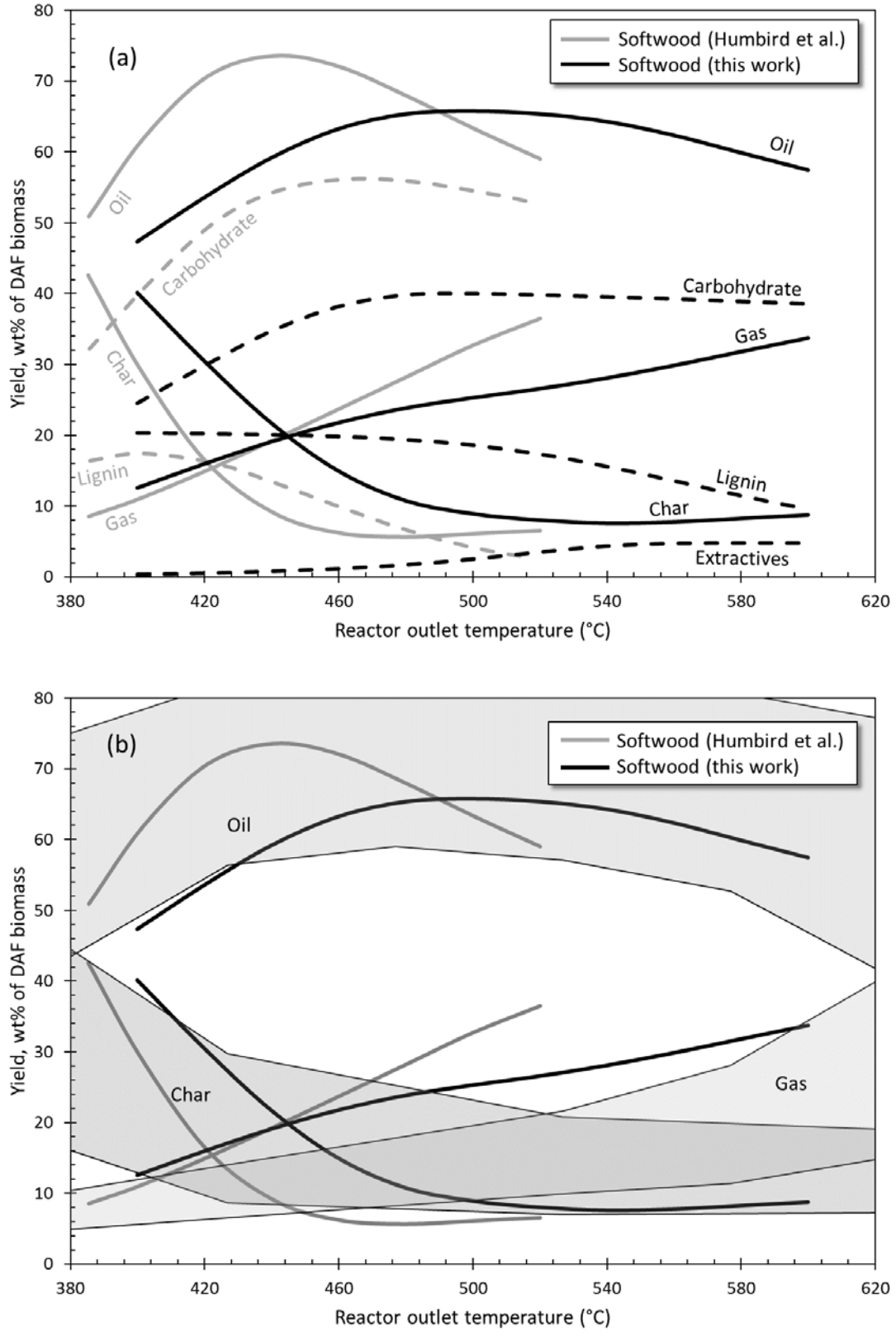

Figure 4 Comparison between oil, gas, and char yields (solid lines) for softwood feedstock as functions of pyrolysis temperature predicted by the Humbird et al. model[8] and the new model. (a) Carbohydrate- lignin- and extractives-derived oil constituents (dashed lines) are also shown. (b) Model results compared to bands of typical experimental yields from Figure 9 in Calonaci et al.[16]

Table 3 Results of parametric sensitivity study. MPS refers to medium-pressure steam, CW and ChW refer to cooling water and chilled water, respectively.

Variable Modified	Process Inputs						Product Distribution (wt% DAF biomass)			Brake Horsepower (kW)		High-Pressure Steam (kW)		MPS (kW)	CW (kW)	ChW (kW)
	Temperature (°C)	Pressure (bar)	Diameter (mm)	Sand/Bio Ratio	Gas/Bio Ratio	DAF Biomass Feed (kg/hr)	Oil	Gas	Solid	CO-01	CO-02	HX-01	HX-06	HX-03	HX-04	HX-05
Baseline	500	2.3	80	10.48	0.51	81.27	65.8	25.3	8.9	8.59	0.74	-51.4	-75.2	-9.31	-14.12	-6.70
Reactor Outlet Temperature	340	2.3	80	10.48	0.51	81.27	30.4	5.3	64.3	8.59	0.56	-167.1	-104.6	0.00*	-5.47	-2.54
	400	2.3	80	10.48	0.51	81.27	47.4	12.5	40.1	8.59	0.64	-122.8	-90.9	-1.60	-8.74	-4.34
	600	2.3	80	10.48	0.51	81.27	57.5	33.8	8.7	8.59	0.90	-59.8	-92.8	-16.44	-14.05	-6.22
	700	2.3	80	10.48	0.51	81.27	52.7	37.8	9.6	8.59	0.97	-59.9	-107.5	-23.57	-13.54	-5.75
Reactor Inlet Pressure	500	1.3	80	10.48	0.51	81.27	60.1	20.9	19.0	2.64	0.79	-65.6	-81.2	-10.01	-10.22	-5.43
	500	1.8	80	10.48	0.51	81.27	63.7	25.3	11.1	5.91	1.03	-55.9	-77.4	-10.07	-12.48	-6.14
	500	2.8	80	10.48	0.51	81.27	64.9	26.9	8.3	10.89	1.15	-54.5	-76.5	-9.22	-14.61	-6.67
	500	3.3	80	10.48	0.51	81.27	63.6	28.3	8.1	12.92	1.53	-58.8	-78.3	-9.18	-14.90	-6.60
Reactor Diameter	500	2.3	48	10.48	0.51	81.27	51.6	8.9	39.5	8.59	0.53	-99.9	-93.4	-7.71	-7.74	-4.33
	500	2.3	64	10.48	0.51	81.27	63.3	19.3	17.5	8.59	0.67	-63.3	-79.3	-8.85	-12.22	-6.05
	500	2.3	96	10.48	0.51	81.27	63.1	28.9	8.0	8.59	0.81	-56.9	-77.8	-9.36	-14.41	-6.64
	500	2.3	112	10.48	0.51	81.27	59.1	32.5	8.5	8.59	0.88	-68.9	-83.1	-9.32	-14.32	-6.36
Sand/Biomass Ratio	500	2.3	80	6.29	0.51	81.27	65.9	25.3	8.9	8.59	0.74	-38.8	-87.7	-9.32	-14.09	-6.68
	500	2.3	80	8.46	0.51	81.27	65.8	25.3	8.9	8.59	0.74	-46.4	-80.2	-9.31	-14.11	-6.69
	500	2.3	80	12.5	0.51	81.27	65.8	25.3	8.9	8.59	0.74	-55.1	-71.4	-9.33	-14.13	-6.71
	500	2.3	80	14.67	0.51	81.27	65.9	25.3	8.9	8.59	0.74	-58.2	-68.3	-9.33	-14.14	-6.72
Gas/Biomass Ratio	500	2.3	80	10.48	0.31	81.27	65.8	26.1	8.2	8.59	0.56	-50.6	-74.6	-9.36	-13.43	-6.89
	500	2.3	80	10.48	0.41	81.27	65.9	25.7	8.4	8.59	0.65	-50.7	-74.8	-9.32	-13.81	-6.81
	500	2.3	80	10.48	0.61	81.27	65.5	24.8	9.8	8.59	0.84	-52.9	-76.0	-9.31	-14.27	-6.54
	500	2.3	80	10.48	0.71	81.27	64.5	23.9	11.6	8.59	0.95	-56.0	-77.4	-9.33	-14.14	-6.29
DAF Biomass Flow Rate	500	2.3	80	10.48	0.51	48.76	61.2	30.6	8.2	8.59	0.51	-19.8	-66.5	-5.60	-8.64	-3.91
	500	2.3	80	10.48	0.51	65.02	64.5	27.4	8.2	8.59	0.62	-33.5	-70.6	-7.48	-11.47	-5.36
	500	2.3	80	10.48	0.51	97.53	65.9	23.4	10.8	8.59	0.86	-74.0	-80.4	-11.03	-16.41	-7.89
	500	2.3	80	10.48	0.51	113.78	64.7	21.2	14.1	8.59	0.96	-102.5	-86.6	-12.64	-18.11	-8.83

*At 340°C the energy needed to preheat the reactor feed is greater than that needed to cool the products to their dew point. No medium-pressure steam is produced while a small amount of heating is required.

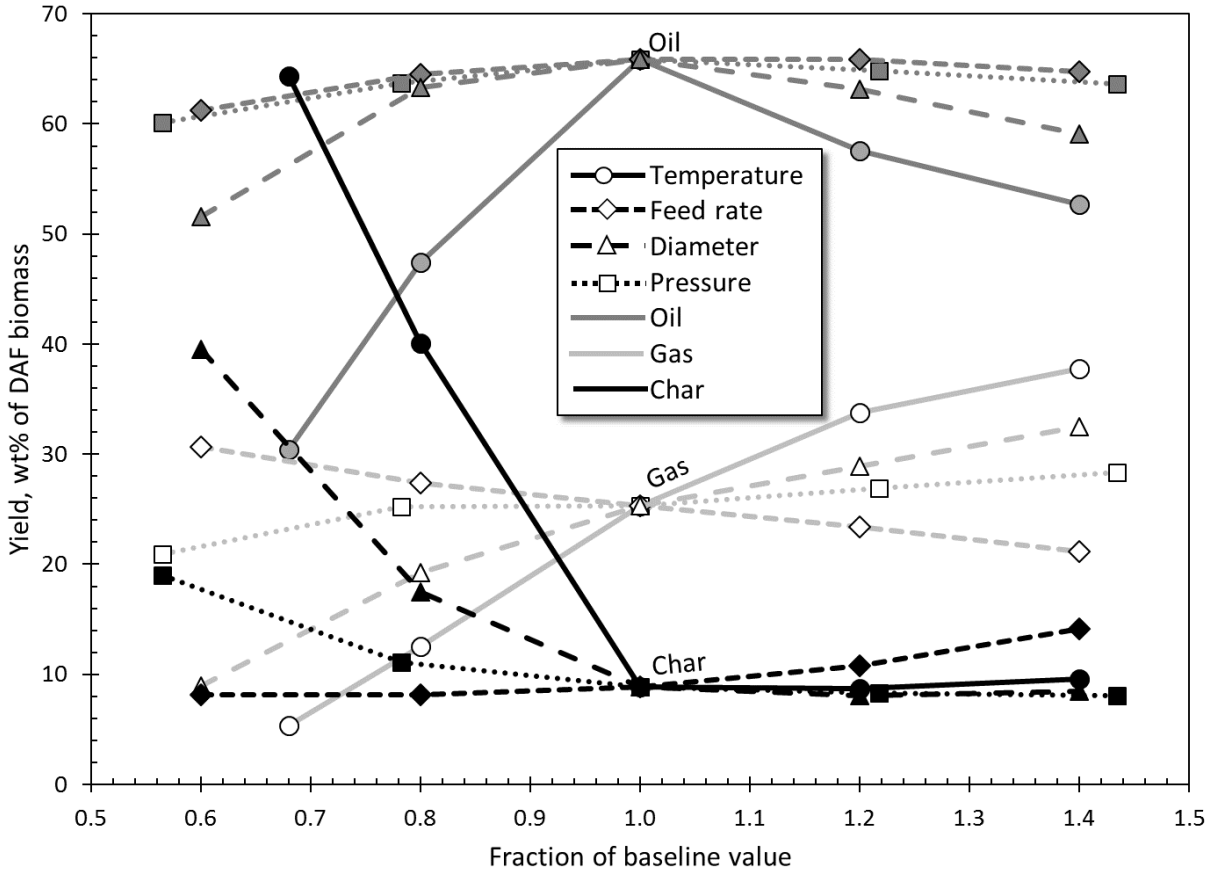

Figure 5 Single-variable effects on organic bio-oil yield. Baseline is 500°C, 2.3 bar, 81.27 kg/hr DAF biomass feed, and reactor inner diameter of 80 mm. Lines do not represent expected curvature but are included to tie related points together. Black lines are for char, darker gray for bio-oil, and lighter gray for gas. Dash/marker types differentiate between temperature, feed rate, diameter, and pressure effects.

Supporting Information

for

A RIGOROUS PROCESS MODELING METHODOLOGY FOR BIOMASS FAST PYROLYSIS WITH AN ENTRAINED-FLOW REACTOR

Benjamin H. Caudle[1,2], Maximilian B. Gorensek[3,*], Chau-Chyun Chen[2]

[1]Savannah River Consulting, LLC, 301 Gateway Dr, Aiken, SC 29803

[2]Department of Chemical Engineering, Texas Tech University, PO Box 43121, Lubbock, TX 79409-3121

[3]Renewable and Nuclear Programs, Savannah River National Laboratory, Savannah River Site, 703-41A/225, Aiken, SC 29808

[*]Phone: +1 803 725-1314. E-mail: maximilian.gorensek@srnl.doe.gov.

11 pages, 4 tables

Reactor model description.

The reactor model is an adaptation of the model published by Humbird et al.[1] A complete description is provided here for the convenience of the reader, much of it copied directly from Humbird et al.,[1]. Changes made to the original model are noted explicitly. The model is one-dimensional, uniform in the radial direction, and varies only in the direction of flow, the vertical, z-direction. Three distinct phases are considered: biomass/char (b), gas (g), and sand (s). The variables that have calculated spatial derivatives are the mass flows of each component, the velocity of each phase, the mass flux of the biomass and gas phases, the enthalpy flux of each phase, and the common pressure. These are the only variables with z-derivatives in the equations below.

Continuity and species mass balance.

Mass fluxes, ϕ_p [kg/(m^2·s)] define the total flow of each phase (p = b for biomass, g for gas, or s for sand phase). They are calculated from the volume fraction, ϵ_p the mass density, ρ_p [kg/m^3] and velocity, v_p [m/s] of each phase.

$$\phi_b = \epsilon_b \rho_b v_b \tag{1}$$

$$\phi_g = \epsilon_g \rho_g v_g \tag{2}$$

$$\phi_s = \epsilon_s \rho_s v_s \tag{3}$$

The sum of the volume fractions must equal unity.

$$\epsilon_b + \epsilon_g + \epsilon_s = 1 \tag{4}$$

Since the sand heat transfer medium is inert, its mass flux is constant along z. However, mass leaves the biomass phase and enters the gas phase as pyrolysis proceeds. The

product of the mass flux and the cross-sectional area of the reactor, A_{cs} [m^2] for the biomass and gas phases must equal the sum of the individual component mass flow rates, $\dot{m}_i$ [kg/s]. For component *i* in the biomass phase and component *j* in the gas phase, the following equalities can be written.

$$\phi_b A_{cs} = \sum_i^{\text{biomass}} \dot{m}_i \tag{5}$$

$$\phi_g A_{cs} = \sum_j^{\text{gas}} \dot{m}_j \tag{6}$$

The density of sand (ρ_s) does not vary significantly with temperature and is assumed to be fixed. While the original model also assumed a fixed density for biomass (ρ_b), this model assumes that biomass density shrinks in proportion to its mass flux, consistent with maintaining a constant diameter (note that ρ_b is not intended to match the actual density of the biomass solids because it includes the effect of intraparticle voids)

$$\rho_b = \rho_{b,0} \frac{\phi_b}{\phi_{b,0}} \tag{7}$$

Here $\rho_{b,0}$ is the initial density [kg/m^3] and $\phi_{b,0}$ the initial mass flux [kg/(m^2·s)] of the biomass. Gas phase density depends on the gas temperature, T_g [K] and local pressure, P [N/m^2] and can be calculated from the ideal gas law (R is the universal gas constant [N·m/(kmol·K)]):

$$\rho_g = \frac{P}{R T_g} \overline{\text{MW}_g} \tag{8}$$

The mean molecular weight of the gas phase can be calculated from the individual component mass flow rates, $\dot{m}_{g,i}$ and molecular weights, MW_i [kg/kmol].

$$\overline{\text{MW}_g} = \frac{\sum_i^{\text{gas}} \dot{m}_{g,i}}{\sum_i^{\text{gas}} \left(\frac{\dot{m}_{g,i}}{\text{MW}_i} \right)} \tag{9}$$

This allows the differential equations for the biomass and gas phase continuity to be written as a set of species continuity equations representing flowing mass loss or gain due to pyrolysis reactions. The rate constants for the pyrolysis reactions proposed by Ranzi et al.[2] have an Arrhenius temperature dependence. For the n^{th} reaction, the rate constant, k_n [s^{-1}] is given by:

$$k_n = A_n T_b^{x_n} \exp\left(-\frac{E_n}{R_k T_b} \right) \tag{10}$$

Here A_n is the pre-exponential coefficient [$K^{-x_n} \cdot s^{-1}$], x_n is the temperature exponent (= 0 or 1, depending on the reaction), E_n is the activation energy [kcal/kmol], and R_k is the universal gas constant [kcal/(kmol·K)]. Values of A_n, x_n, and E_n for the 21 reactions used in this model are listed in Table 1 of the manuscript. All 21 reactions are decompositions of individual biomass phase components and first-order with respect to that component. Consequently, the biomass temperature, T_b is the temperature used for calculating rate constants, and the rate per unit height in the z-direction of the n^{th} reaction, R_n [kg/(m·s)] is given by:

$$R_n = \frac{\dot{m}_n}{v_\text{b}} k_n \tag{11}$$

Here $\dot{m}_n$ is the mass flow rate of the component being consumed in the n^{th} reaction. Putting this all together, the continuity equation for component i in the biomass and the gas phase is the sum of all its reaction rates. Therefore, for N (= 21) total reactions:

$$\frac{\mathrm{d}}{\mathrm{d}z}\dot{m}_i = \sum_{n=1}^{N} \nu_{n,i} R_n \frac{\mathrm{MW}_i}{\mathrm{MW}_n} \tag{12}$$

where $\nu_{n,i}$ is the stoichiometric coefficient of the i^{th} component in the n^{th} reaction, and MW_n is the molecular weight of the component being consumed by the n^{th} reaction.

With the velocity of each phase established, it is possible to calculate the residence time of each phase, τ_p, with numerical integration. For K (=154) total segments with individual lengths l_k:

$$\tau_p = \sum_{k=1}^{K} \frac{l_k}{v_{p,k}} \tag{13}$$

Momentum transfer.

The driving force for carrying the biomass and sand phases in the z-direction is the fluidizing gas. The model considers buoyancy and gravity forces as well as momentum transfer between the gas phase and each solid phase. Momentum transfer between the two solid phases due to interparticle collisions is also included. The differential equations governing momentum transfer are shown below:

Biomass phase:

$$\frac{\mathrm{d}}{\mathrm{d}z}\phi_\text{b} v_\text{b} = -\epsilon_\text{b}\frac{\mathrm{d}P}{\mathrm{d}z} - \epsilon_\text{b}\rho_\text{b} g + I_{\text{g-b}}\left(v_\text{g} - v_\text{b}\right) + F_{\text{s-b}}(v_\text{s} - v_\text{b}) \tag{14}$$

Gas phase:

$$\frac{\mathrm{d}}{\mathrm{d}z}\phi_\text{g} v_\text{g} = -\epsilon_\text{g}\frac{\mathrm{d}P}{\mathrm{d}z} - \epsilon_\text{g}\rho_\text{g} g + I_{\text{g-b}}\left(v_\text{b} - v_\text{g}\right) + I_{\text{g-s}}\left(v_\text{s} - v_\text{g}\right) \tag{15}$$

Sand phase:

$$\frac{\mathrm{d}}{\mathrm{d}z}\phi_{\mathrm{s}}v_{\mathrm{s}} = -\epsilon_{\mathrm{s}}\frac{\mathrm{d}P}{\mathrm{d}z} - \epsilon_{\mathrm{s}}\rho_{\mathrm{s}}g + I_{\mathrm{g-s}}\left(v_{\mathrm{g}} - v_{\mathrm{s}}\right) + F_{\mathrm{s-b}}(v_{\mathrm{b}} - v_{\mathrm{s}}) \tag{16}$$

Here g is the acceleration due to gravity (9.81 m/s^2). Gas-solid momentum transfer for solid phase m is calculated using a multiparticle drag coefficient, $I_{\mathrm{g-m}}$ [kg/(m^3·s)]:

$$I_{\mathrm{g-m}} = \frac{3}{4}\frac{C_{\mathrm{D,m}}\epsilon_{\mathrm{g}}\epsilon_{\mathrm{m}}\rho_{\mathrm{g}}}{d_{\mathrm{m}}}\left|v_{\mathrm{g}} - v_{\mathrm{m}}\right| \tag{17}$$

Here d_{m} [m] is the characteristic particle diameter in solid phase m and the dimensionless multiparticle drag coefficient, $C_{\mathrm{D,m}}$ is a function only of the dimensionless terminal velocity of the solid particles, $V_{r,\mathrm{m}}$ and their Reynolds number (based on the gas properties and gas slip velocity with solid phase m):

$$C_{\mathrm{D,m}} = \frac{\left(0.63 + 4.8\sqrt{V_{r,\mathrm{m}}/\mathrm{Re}_{\mathrm{m}}}\right)^2}{V_{r,m}^2} \tag{18}$$

The dimensionless terminal velocity of the solid particles in phase m is a function only of their Reynolds number and their volume fraction:

$$V_{r,\mathrm{m}} = 0.5\left(A - 0.06\mathrm{Re}_{\mathrm{m}} + \sqrt{(0.06\mathrm{Re}_{\mathrm{m}})^2 + 0.12\mathrm{Re}_{\mathrm{m}}(2B - A) + A^2}\right) \tag{19}$$

$$A = \epsilon_{\mathrm{g}}^{4.14} \tag{20}$$

$$B = -9.0071\epsilon_{\mathrm{g}}^6 + 35.889\epsilon_{\mathrm{g}}^5 - 50.951\epsilon_{\mathrm{g}}^4 + 33.370\epsilon_{\mathrm{g}}^3 - 10.236\epsilon_{\mathrm{g}}^2 + 2.0251\epsilon_{\mathrm{g}} - 0.0874 \tag{21}$$

$$\mathrm{Re}_{\mathrm{m}} = \frac{d_{\mathrm{m}}\rho_{\mathrm{g}}\left|v_{\mathrm{g}} - v_{\mathrm{m}}\right|}{\mu_{\mathrm{g}}} \tag{22}$$

Here μ_{g} is the gas phase viscosity [Pa·s]. The sand-biomass momentum transfer term also makes use of a drag coefficient, $F_{\mathrm{s-b}}$ [kg/(m^3·s)]:

$$F_{\mathrm{s-b}} = 3(1 + \epsilon_{\mathrm{s-b}})\left(\frac{\pi}{2} + c_{f,\mathrm{s-b}}\frac{\pi^2}{8}\right)\frac{(d_{\mathrm{s}} + d_{\mathrm{b}})^2}{2\pi\left(\rho_{\mathrm{s}}d_{\mathrm{s}}^3 + \rho_{\mathrm{b}}d_{\mathrm{b}}^3\right)}\epsilon_{\mathrm{s}}\rho_{\mathrm{s}}\epsilon_{\mathrm{b}}\rho_{\mathrm{b}}g_{\mathrm{s-b}}^0\left|v_{\mathrm{s}} - v_{\mathrm{b}}\right| \tag{23}$$

This correlation includes a dimensionless coefficient of restitution, $\epsilon_{\mathrm{s-b}} = 0.9$ and a dimensionless particle friction coefficient, $c_{f,\mathrm{s-b}} = 0.0001$.[3] The dimensionless radial distribution function for contacting hard spheres, $g_{\mathrm{s-b}}^0$, is given by:

$$g_{\mathrm{s-b}}^0 = \frac{1}{\epsilon_{\mathrm{g}}} + \frac{3d_{\mathrm{s}}d_{\mathrm{b}}}{\epsilon_{\mathrm{g}}^2(d_{\mathrm{s}} + d_{\mathrm{b}})}\left(\frac{\epsilon_{\mathrm{s}}}{d_{\mathrm{s}}} + \frac{\epsilon_{\mathrm{b}}}{d_{\mathrm{b}}}\right) \tag{24}$$

Heat transfer.

As in the original model, since the actual volume fractions of sand and biomass are much smaller than that of the gas phase, it is assumed that heat is transferred between the two solid phases only through the gas phase. Thus, the model accounts for heat transfer between gas and biomass and between gas and sand but ignores direct heat transfer between the two solid phases. However, this model treats the reaction heat effects very differently than the original. Instead of estimating the heats of reaction for all 21 reactions and using them in conjunction with heat capacities to calculate temperature changes, it performs a differential enthalpy balance. The differential equations governing heat transfer are shown below:

Biomass phase:

$$\frac{\mathrm{d}Q_\mathrm{b}}{\mathrm{d}z} = h_{\mathrm{b-g}}\left(T_\mathrm{g} - T_\mathrm{b}\right) - \sum_{i}^{\substack{\text{all volatile}\\ \text{products}}} h_i^* \frac{\mathrm{d}}{\mathrm{d}z}\dot{m}_{\mathrm{g},i} \tag{25}$$

$$Q_\mathrm{b} = H_\mathrm{b}\phi_\mathrm{b} \tag{26}$$

Gas phase:

$$\frac{\mathrm{d}Q_\mathrm{g}}{\mathrm{d}z} = h_{\mathrm{s-g}}\left(T_\mathrm{s} - T_\mathrm{g}\right) + h_{\mathrm{b-g}}\left(T_\mathrm{b} - T_\mathrm{g}\right) + \sum_{i}^{\substack{\text{all volatile}\\ \text{products}}} h_i^* \frac{\mathrm{d}}{\mathrm{d}z}\dot{m}_{\mathrm{g},i} \tag{27}$$

$$Q_\mathrm{g} = H_\mathrm{g}\phi_\mathrm{g} \tag{28}$$

Sand phase:

$$\frac{\mathrm{d}Q_\mathrm{s}}{\mathrm{d}z} = h_{\mathrm{s-g}}\left(T_\mathrm{g} - T_\mathrm{s}\right) \tag{29}$$

$$Q_\mathrm{s} = H_\mathrm{s}\phi_\mathrm{s} \tag{30}$$

where Q_b, Q_g, and Q_s are the enthalpy fluxes [W/m^2] of the biomass, gas, and sand phases, respectively and H_b, H_g, and H_s are the mass enthalpies [J/kg] of the biomass, gas, and sand phases, respectively, which are functions of local phase temperature, pressure, and composition and can be calculated from the properties model. The pure component mass enthalpy of volatile species i, h_i^* [J/kg] is also calculated from the properties model at the temperature of the biomass phase from which it is released. The variable $\dot{m}_{\mathrm{g},i}$ is the mass flow rate [kg/s] of species i in the gas phase. Finally, $h_{\mathrm{s-g}}$ and $h_{\mathrm{b-g}}$ are the heat transfer coefficients per unit height [W/(m^3·K)] for sand-to-gas and biomass-to-gas heat transfer, respectively, and T_b, T_g, and T_s are the temperatures of the biomass, gas, and sand phases, respectively [K]. The heat transfer coefficient for solid phase m is given by:

$$h_{\mathrm{m-g}} = \frac{6k_\mathrm{g}\epsilon_\mathrm{m}}{{d_\mathrm{s}}^2}\,\mathrm{Nu}_\mathrm{m} \tag{31}$$

where k_g is the thermal conductivity [W/(m·K)] of the gas phase and Nu_m is the Nusselt number for solid phase m. This restores the exponent in the denominator that was inadvertently omitted by Humbird et al.[1] (see Trendewicz[3] for the correct correlation). The Nusselt number is calculated using the following correlation:

$$\mathrm{Nu_m} = 1.9019\left(1 + 0.3136\mathrm{Re_m^{0.2}Pr_g^{0.33}} + 0.0185\mathrm{Re_m^{0.7}Pr_g^{0.33}}\right) \tag{32}$$

Here Pr_g is the Prandtl number, which can be calculated from gas phase properties:

$$\mathrm{Pr_g} = \frac{C_{P,g}\mu_g}{k_g} \tag{33}$$

where $C_{P,g}$ is the gas phase heat capacity [kJ/(kg·K)].

Model set-up

As noted in the manuscript, the same laboratory-scale reactor (4-m long, 8-cm inside diameter) is simulated as in Humbird et al.'s work.[1] However, the discretization uses a finer grid, also noted in the manuscript, resulting in 155 nodes (or 154 segments) with much tighter spacing closer to the inlet. The equations presented above are solved at each node using steady-state distributed variables.

Boundary conditions that need to be specified include the individual component feed rates and the inlet temperature for each phase, the pressure at the inlet, the initial density of the biomass phase, and either inlet velocities or volume fractions for two of the three phases. Other variables that need to be set are the particle diameters for the sand and biomass phases, and the viscosity and thermal conductivity of the gas phase.

For this work, the reactor model was set up using Aspen Custom Modeler (ACM), although any equation-solving simulation platform with the ability to perform thermophysical properties calculations for process streams could be used instead.

Solution method.

Stream data from the steady-state flowsheet simulator is used to set up the boundary conditions (feed stream specifications) for the 1-D reactor model. For this work, Aspen Plus was used to model the flowsheet, although any process flowsheet simulator could be used instead. The Aspen Simulation Workbook add-in for Microsoft Excel is used to create dynamic links between the flowsheet and reactor models through a spreadsheet to manage data transfer between the models. Reasonable initial estimates are needed to ensure timely convergence of the two models to a common solution. The equations that comprise the 1-D reactor model are solved simultaneously by ACM. The enthalpies in equations (25) through (30) are functions of the phase temperatures, so the solver find the values of T_b, T_g, and T_s that satisfy these relationships.

Once the 1-D reactor model converges, the extents of all the pyrolysis reactions are calculated from the results and entered along with the outlet pressure into a stoichiometric reactor block representing the pyrolysis reactor in the steady-state flowsheet simulator. This block calculates the pyrolysis product composition from the reaction extents and the temperature from an energy balance. The steady-state simulator is run and a new set of

feed stream specifications for the 1-D reactor model generated. The process is repeated until the changes from one iteration to the next fall within convergence criteria. When converged, the results of the stoichiometric reactor model (feed and product stream compositions, flow rates, temperatures, and pressures) should match those of the 1-D reactor model.

Base case

The base case for this work attempts to match the base case in Humbird et al.,[1] although the biomass feed composition is different because of the presence of extractives. The compositions of the biomass materials used in this work and in the previous work by Humbird et al.[1] are shown in Table 1 below. Note that the base case uses softwood as the feedstock. Humbird et al.[1] did not differentiate between hardwood and softwood hemicelluloses nor did they consider extractives. This work used compositions for Douglas fir (Softwood) and summer switchgrass (Switchgrass) from the Supporting Information for Calonaci et al.[4] based on their similar compositions.

Table 1 Biomass compositions used in fast pyrolysis simulations (moisture-free basis)

	Softwood		**Switchgrass**	
Component	**Humbird et al.[1]**	**This work[4]**	**Humbird et al.[1]**	**This work[4]**
Cellulose (CELL)	0.4592	0.4385	0.4673	0.4152
Glucomannan (GMSW)	0.2653	0.2191	0.2804	0.0000
Xylan (XYHW)		0.0000		0.2909
High-C Lignin (LIGC)	0.0898	0.0471	0.0696	0.0103
High-H Lignin (LIGH)	0.0898	0.1199	0.0696	0.0019
High-O Lignin (LIGO)	0.0888	0.1084	0.0696	0.1654
Triglyceride (TGL)		0.0499		0.0291
Tannin (TANN)		0.0125		0.0603
Ash (ASH)	0.0071	0.0046	0.0436	0.0269
Sum	1.0000	1.0000	1.0000	1.0000

The boundary conditions for the base case simulation in this work are listed in Table 2 below.

Table 2 Boundary/inlet conditions used for base case simulation

Description	**Value**
Initial sand velocity (m/s)	0.15
Initial biomass velocity (m/s)	0.15
Sand particle diameter (mm)	0.5
Biomass particle diameter (mm)	0.5
Sand density (kg/m^3)	2580
Initial biomass density (kg/m^3)	650

Description	Value
Gas viscosity (cP)	0.0312
Gas thermal conductivity W/(m·K)	0.07

Specifications for the unit operations that comprise the base case process flowsheet are shown in Table 3 below.

Table 3 Block specifications for base case flowsheet simulation

Block ID	Block type	Parameter	Value
CO-01	Compressor	Outlet pressure (bar) Isentropic efficiency (%)	2.34 85
CO-02	Compressor	Outlet pressure (bar) Isentropic efficiency (%)	2.55 85
CY-01	Component separator	Gaseous species overhead (%) Biomass intermediates overhead (%) Other solids overhead (%)	100 99.9 0.1
CY-02	Component separator	Solid species removal (%)	99.9
HX-01	Heater	Outlet temperature (°C)[a] Pressure drop (bar)	480-740 0.03
HX-02	Heat exchanger	Cold side outlet temperature (°C) Pressure drops (bar)	395 0.25
HX-03	Heater	Degrees of superheat (°C) Pressure drop (bar)	1 0.25
HX-04	Heater	Outlet temperature (°C) Pressure drop (bar)	40 0.045
HX-05	Heater	Outlet temperature (°C) Pressure drop (bar)	16 0.045
HX-06	Heater	Outlet temperature (°C) Outlet pressure (bar)	98 1.013
RX-01	Stoichiometric reactor[b]	Heat duty (kW) Pressure drop (bar) Reaction extents from ACM model	0 0.02
RX-02	Hierarchy block[c]	Stoichiometric reactor heat duty (kW) Outlet pressure (bar) Complete combustion Sand to solids outlet (%)	0 0.02 99.9
SP-01	Stream splitter	Recycle ratio	0.9

[a] Adjusted to achieve desired pyrolysis reactor outlet temperature.

[b] The pressure drop and the extents of all 21 reactions are obtained from the ACM reactor model.

[c] The char combustor is modeled with a stoichiometric reactor that completely combusts all carbon- and hydrogen-containing species to CO_2 and H_2O and a subsequent component separator that recovers 99.9% of the sand as feed to HX-01 while passing everything else to CY-02.

Block ID	Block type	Parameter	Value
SP-02	Stream splitter	Recycle rate (kg/h)	41.64

The base case feed stream specifications are detailed in Table 4 below.

Table 4 Feed stream specifications for base case simulation

Stream 01 – Raw biomass	
Temperature (°C)	100
Pressure (bar)	2.3
Vapor/liquid flow rate (kg/h)	5.74
TGL (wt%)	70.97
H2OL (wt%)	29.03
Solids flow rate (kg/h)	77.58
TANN (wt%)	1.32
LIGC (wt%)	4.96
LIGH (wt%)	12.62
LIGO (wt%)	11.41
GMSW (wt%)	23.06
XYHW (wt%)	0.00
CELL (wt%)	46.15
ASH (wt%)	0.48
Stream 02 – Make-up sand	
Temperature (°C)	25
Pressure (bar)	2.3
Flow rate (kg/h)	1.7
Stream 03 – Air to combustor	
Temperature (°C)	25
Pressure (bar)	1.013
Flow rate (kg/h)	325
AR (mol%)	0.93
CO2 (mol%)	0.04
N2 (mol%)	78.09
O2 (mol%)	20.95

Nomenclature

Symbol	Description	Units
	Latin symbols	
A	Dimensionless function of gas phase volume fraction	
A_{cs}	Reactor cross-sectional area	m^2

Symbol	Description	Units
A_n	Rate pre-exponential coefficient for reaction n	$K^{-x_n} \cdot s^{-1}$
B	Dimensionless function of gas phase volume fraction	
$C_{D,m}$	Dimensionless drag coefficient	
$c_{f,s-b}$	Dimensionless particle friction coefficient	
$C_{P,g}$	Gas phase heat capacity	kJ/(kg·K)
d_m	Characteristic particle diameter in solid phase m	m
E_n	Activation energy for reaction n	kcal/kmol
F_{s-b}	Multiparticle sand-biomass drag coefficient	$kg/(m^3 \cdot s)$
g	Acceleration due to gravity	m/s^2
g^0_{s-b}	Dimensionless radial distribution function for contacting hard spheres	
h_{m-g}	Heat transfer coefficient per unit height for solid-phase-m-to-gas heat transfer	$W/(m^3 \cdot K)$
H_p	Mass enthalpy of phase p	J/kg
h_i^*	Pure component mass enthalpy of volatile species i	J/kg
I_{g-m}	Multiparticle gas-solid drag coefficient	$kg/(m^3 \cdot s)$
k_g	Gas phase thermal conductivity	W/(m·K)
k_n	Rate constant for reaction n	s^{-1}
l_k	Length of a given reactor segment	m
$\dot{m}_i$	Mass flow rate of component i	kg/s
$\dot{m}_n$	Mass flow rate of decomposing species in n^{th} reaction	kg/s
$\dot{m}_{p,i}$	Mass flow rate of component i in phase p	kg/s
MW_i	Molecular weight of component i	kg/kmol
MW_n	Molecular weight of decomposing species in n^{th} reaction	kg/kmol
$\overline{MW_p}$	Mean molecular weight of phase p	kg/kmol
N	Total number of pyrolysis reactions	
Nu_m	Nusselt number in solid phase m	
P	Pressure	N/m^2
Pr_g	Prandtl number in the gas phase	
Q_p	Enthalpy flux of phase p	W/m^2
R	Universal gas constant	N·m/(kmol·K)
R_k	Universal gas constant	kcal/(kmol·K)
R_n	Rate per unit height of n^{th} reaction	kg/(m·s)
Re_m	Particle gas slip Reynolds number in solid phase m	
T_p	Temperature of phase p	K
v_p	Velocity of phase p	m/s
$V_{r,m}$	Dimensionless particle terminal velocity in solid phase m	
x_n	Rate pre-exponential temperature exponent for reaction n	
z	Height above reactor inlet	m
	Greek symbols	
ϵ_p	Volume fraction of phase p	
ϵ_{s-b}	Dimensionless coefficient of restitution	

Symbol	Description	Units
μ_g	Gas phase viscosity	Pa·s
$\nu_{n,i}$	Stoichiometric coefficient of i^{th} species in n^{th} reaction	
$\rho_{b,0}$	Initial mass density of biomass phase	kg/m^3
ρ_p	Mass density of phase p	kg/m^3
τ_p	Residence time of phase p	s
$\phi_{b,0}$	Mass flux of biomass phase at reactor inlet	kg/(m^2·s)
ϕ_p	Mass flux of phase p	kg/(m^2·s)

Subscripts

b	Biomass phase
g	Gas phase
i, j	Component identification
k	Reactor segment identification
m	Solid phase identification
n	Reaction identification
p	Phase identification
s	Sand phase
0	Inlet condition

References

1. Humbird D, Trendewicz A, Braun R, Dutta A. One-Dimensional Biomass Fast Pyrolysis Model with Reaction Kinetics Integrated in an Aspen Plus Biorefinery Process Model. *ACS Sustainable Chemistry & Engineering.* 2017/03/06 2017;5(3):2463-2470.

2. Ranzi E, Debiagi PEA, Frassoldati A. Mathematical Modeling of Fast Biomass Pyrolysis and Bio-Oil Formation. Note I: Kinetic Mechanism of Biomass Pyrolysis. *ACS Sustainable Chemistry & Engineering.* 2017/04/03 2017;5(4):2867-2881.

3. Trendewicz AA. *Development of a circulating fluidized bed reactor model for the fast pyrolysis of biomass for process simulation*. Golden, CO: Department of Mechanical Engineering, Colorado School of Mines; 2015.

4. Calonaci M, Grana R, Barker Hemings E, Bozzano G, Dente M, Ranzi E. Comprehensive Kinetic Modeling Study of Bio-oil Formation from Fast Pyrolysis of Biomass. *Energy & Fuels.* 2010/10/21 2010;24(10):5727-5734.